

Raman-LIF Measurements of Temperature, Major Species, OH, and NO in a Methane–Air Bunsen Flame

Q. V. NGUYEN* and R. W. DIBBLE

Department of Mechanical Engineering, University of California, Berkeley, CA 94720

C. D. CARTER

Systems Research Laboratories, Inc., 2800 Indian Ripple Road, Dayton, OH 45440-3696

G. J. FIECHTNER and R. S. BARLOW

Combustion Research Facility, Sandia National Laboratories, Department 8351, MS 9051, Livermore, CA 94551

Nonintrusive measurements of temperature, the major species (N_2 , O_2 , H_2 , H_2O , CO_2 , CO , CH_4), OH, and NO in an atmospheric pressure, laminar methane–air Bunsen flame were obtained using a combination of Raman–Rayleigh scattering and laser-induced fluorescence. Radial profiles were measured at three axial locations for an equivalence ratio of 1.38. Measurements along the centerline of the flame, for equivalence ratios of 1.38, 1.52, and 1.70, were also obtained. The measurements indicate that the inner unburned fuel–air mixture experiences significant preheating as it travels up into the conical flame zone surrounding it. Consequently, the centerline axial temperatures were typically 100–150 K higher than predicted by adiabatic equilibrium for reactants at an initial temperature of 300 K. Because the amount of preheating increases with the equivalence ratio (due to the increased inner flame height), the maximum temperatures (2000 K) in a Bunsen flame were rather insensitive to the stoichiometry. We observed a 20% reduction of the maximum NO concentrations (80 ppm) in a Bunsen flame by increasing the equivalence ratio from 1.38 to 1.70. We also find that using a one-dimensional premixed laminar flame model incorporating finite-rate chemistry, satisfactorily predicts properties such as the temperature, CO, OH, and NO concentrations at the inner flame.

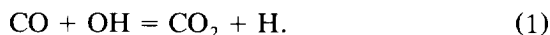
INTRODUCTION

Natural gas, predominantly composed of methane, is an abundant and relatively clean-burning fossil fuel. Its increasing use as the fuel of choice for power generation, industrial process heating, and residential use has been prompted by recently imposed, low-pollutant emissions standards [1]. A large portion of the natural gas consumed in the United States is burned in atmospheric pressure Bunsen flames, characterized by an inner rich premixed flame, followed by an outer zone of nonpremixed combustion. The Bunsen flame, invented in 1855, is referred to as an “atmospheric shot burner” by the gas appliance industry and is used in a predominant number of burner designs for its inherent stability and passively reliable operation, important considerations for residential and commercial gas appliances.

The goal of developing cleaner and more efficient burners is most effectively realized with the aid of a numerical model of the combustion process, allowing manufacturers of natural gas burners to answer exploratory “what if?” questions on a computer. This approach reduces the reliance of the cut-and-try technique, which is becoming increasingly expensive and time consuming. The development of accurate numerical models of combustion, however, require a high-degree of understanding of the interaction between the complex, finite-rate chemistry and multidimensional fluid dynamics. The extent of this understanding is best verified through a direct comparison of the model results with experimental measurements of properties such as temperature and species concentrations. A recent example of this type of comparison was reported by Norton et al. [2] for a rectangular non-premixed methane–air flame. A goal of this paper is to provide an accurate database for comparisons with comprehensive numerical models of laminar premixed methane–air Bunsen flames.

*Corresponding author. Current address: Quang-Viet Nguyen, Combustion Research Facility, Sandia National Laboratories, Dept. 8351, MS 9051, Livermore, CA 94551.

Measurements using traditional techniques such as thermocouples and gas sampling probes, while useful for certain applications, are limited by their intrusiveness when used in flames. Besides perturbing the flow field, thermocouples, require radiative corrections which can introduce a large source of uncertainty in the temperature measurement. Species measurements using gas sampling probes cannot measure the highly reactive combustion intermediates such as the hydroxyl radical (OH), a participant in the reaction



This is one of the most important reactions in the oxidation mechanism of hydrocarbon fuels [3, 4]. In lean-premixed natural gas based flames, sampling probes can also introduce errors to the measurement of carbon monoxide (CO), as previously shown by Nguyen et al. [5].

In addition to the measurement of CO and OH, the accurate measurement of nitric oxide (NO) is of interest due to its toxicity and role in air pollutant formation [6]. The production of NO in combustion processes arises from several different mechanisms (see Refs. 7–10 for a discussion of these mechanisms). The measurement of NO in premixed hydrocarbon fuel flames has been investigated by Bachmeier et al. [11] using probe-sampling techniques. More recent nonintrusive studies of NO in flames include the work of Thorne et al. [12], who examined HC-NO interactions, Drake et al. [10], who examined high-pressure lean premixed flames, Heard et al. [13], who examined the role of radicals in the formation of prompt-NO, and Reisel and Laurendeau [14], who examined the NO production in high-pressure $\text{C}_2\text{H}_6\text{-N}_2\text{-O}_2$ flames. Nonintrusive and quantitative measurements of NO in atmospheric pressure fuel-rich Bunsen flames, to our knowledge, however, have not been reported.

EXPERIMENTAL APPROACH AND APPARATUS

Nonintrusive, optical measurements of temperature and concentration were obtained using laser Raman and Rayleigh scattering, and laser-induced fluorescence (LIF). Raman and

Rayleigh scattering have been previously applied with success to spatially and temporally resolved measurements of temperature and mixture fraction in turbulent non-premixed methane-air flames [15]. LIF is a sensitive technique for detecting trace species such as OH and NO in the parts per million (ppm) range. Recently, Barlow and Carter [16] have demonstrated simultaneous measurements of OH and NO in turbulent nonpremixed hydrogen-air jet flames. The recent success of LIF as a quantitative technique, can be largely attributed to the efforts of Crosley [17], Heard et al. [18], Thoman et al. [19], Drake and Ratcliffe [20], and Paul et al. [21] in measuring the cross-sections for the electronic quenching of OH and NO by numerous colliders. Although a recently demonstrated technique allows a direct mapping of the two-dimensional collisional quenching of OH in low-pressure (0.5 atm) Bunsen flames [22], application of this technique for atmospheric pressure flames is made more difficult by the shorter fluorescence decay times. We have applied the technique used by Carter and Barlow [23], for the measurement of the temperature, and concentrations of the major species, OH, and NO, in a laminar, premixed, methane-air, Bunsen flame.

In particular, we have measured the temperature and concentrations of N_2 , O_2 , H_2O , CO_2 , CO, H_2 , and CH_4 using a combination of Raman and Rayleigh scattering. The Rayleigh scattering cross-section is typically about three orders of magnitude greater than Raman scattering cross-section, and thus Rayleigh scattering provides greater precision in the measurement of the number density. However, Raman scattering measurements are needed to provide an overall Rayleigh scattering cross-section, required for determining the total number density of the gases in the probe volume. The temperature is then calculated through the perfect gas law. The measurements of the major species and temperature also serve a second purpose: they provide the necessary information for the determination of an overall collisional electronic quench rate, which is required for determining the quantitative concentrations of OH and NO from measurements of their respective LIF signals.

The experiments were performed using the Raman-LIF apparatus in the Turbulent Diffusion Flame laboratory within the Combustion Research Facility at Sandia National Laboratory. The details of this apparatus are described by Dibble et al. [15], Barlow and Carter [16], and Barlow et al. [24]. Modifications and improvements to this apparatus, however, are described in this paper.

Burner and Flow Conditions

Figure 1 shows a schematic of the Bunsen burner used in the experiment and the axial locations of the measurements. The burner is similar to the one described by Nguyen et al. [25] and consists of an 82-cm-long, 17-mm-diameter stainless-steel tube surrounded by a 70-mm-diameter honeycomb coflow matrix, which stabilizes the flame from the effects of buoyancy. The long length of the tube assures a condition of fully developed laminar pipe flow at the exit, defining the velocity field for numerical simulations. Pressure regulators control the flows of fuel (bottled CH₄) and dry-air through calibrated orifice plate meters, which are fitted with precision digital manometers. A static mixer then homogenizes the fuel and air flows, providing a steady premixed fuel-to-air ratio. Table 1 shows the operating conditions of the burner for the present study.

Raman and Rayleigh Diagnostics

Figure 2 shows a schematic of the Raman-LIF apparatus. The Bunsen burner is mounted in a vertical wind tunnel, providing filtered air to minimize laser light scattered by dust particles. Stepper motors translate the wind tunnel for spatial profile measurements. For the Raman and Rayleigh scattering measurements, light

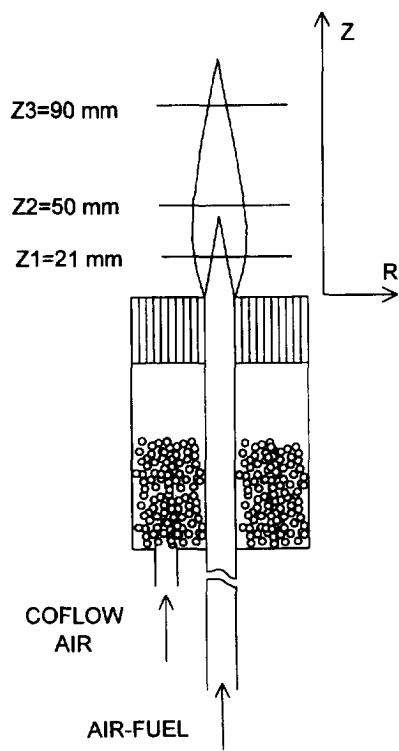


Fig. 1. Schematic of the Bunsen burner used in this study. The coflow air is homogenized by glass beads prior to entering the honeycomb flow straightener. The measurement planes for the radial traverses of flame A are shown.

from a frequency-doubled Nd:YAG laser (532-nm, 10-ns, 700-mJ) was temporally “stretched” to a series of lower energy pulses with an approximate overall width of 100 ns. The longer pulse width reduces the peak laser power, eliminating the breakdown of the gases in the measurement probe volume. The pulse stretcher consists of ten mirrors and two beam-splitter-combiners. The beamsplitters divert fractions of the laser pulse to an optical delay line and subsequently recombine the multiple delayed pulses to a single, longer pulse. Using a 2-m focal length spherical lens, the light

TABLE 1
Premixed Methane–Air Bunsen Flame Operating Conditions

Flame	Traverse	Equivalence Ratio	CH ₄ (slm)	Air (slm)	Coflow (slm)	Inner Flame Height (mm)
A	Radial, Axial	1.38	0.97	6.69	82	42
B	Axial	1.52	1.05	6.63	82	55
C	Axial	1.70	1.17	6.57	82	78

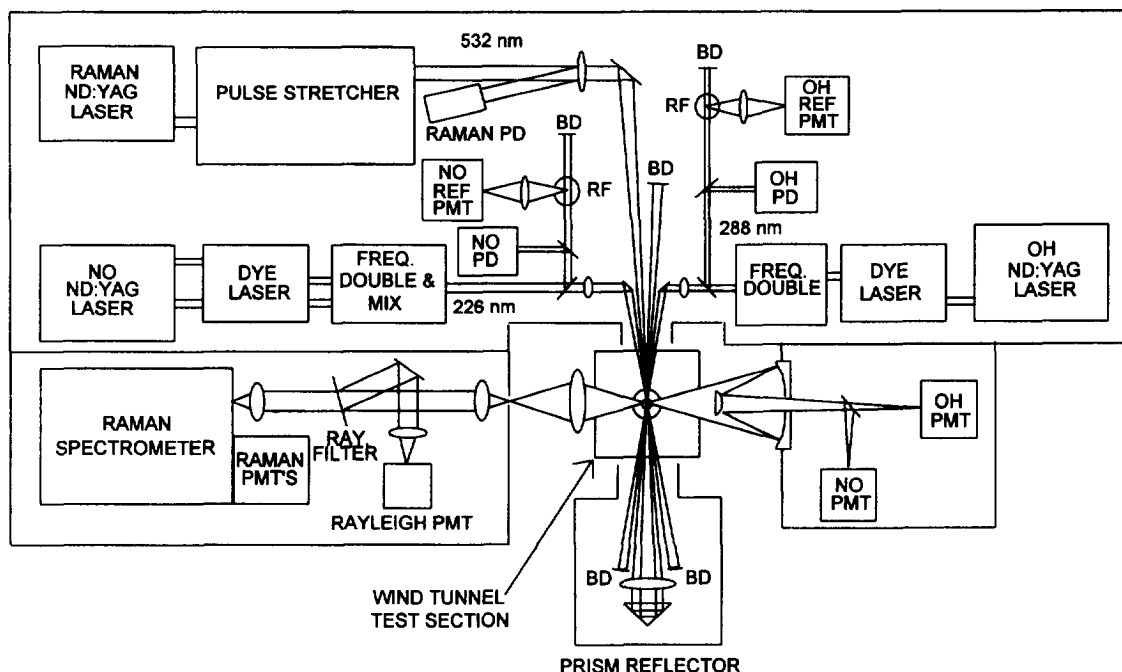


Fig. 2. Schematic of the Raman-Rayleigh-LIF apparatus. Light-tight sheet metal enclosures reduce the background scattered radiation and isolate the laser systems from the collection systems. Legends: BD = beam dump, RF = reference flame, PD = photodiode, PMT = photomultiplier tube.

emerging from the pulse stretcher is focused to a $750\text{-}\mu\text{m}$ beam waist at the probe volume. A small fraction of light reflected from antireflection coating of this lens is directed to a photodiode detector for an energy measurement. The beam, after passing through the probe volume, is then reflected back into the probe volume using a collimating lens and a right-angle prism; this effectively doubles the laser energy in the probe volume. The probe volume dimensions ($750\text{ }\mu\text{m}$ in diameter \times $750\text{ }\mu\text{m}$ long) were defined by the beam waist diameter and the field-stop slit widths of the collection optics.

The Raman and Rayleigh light scattered from the probe volume is collected with a specially designed low f -number achromatic lens [15] and is then collimated with a camera lens. After collimation, a holographic Raman edge filter reflects the Rayleigh scattered light, while transmitting the Raman scattered light. The Rayleigh scattered portion of the beam is then focused onto a slit placed before a photomultiplier tube (PMT) for detection. An achromatic lens (f -number matched to the spec-

trometer) focuses the collimated Raman beam onto the entrance slit of a $3/4\text{-m}$ spectrometer fitted with an 1800 line/mm holographic grating. An achromatic $1/2\text{-}\lambda$ waveplate mounted behind the slits of the spectrometer rotates the vertically polarized Raman beam to a horizontal plane, which is the optimum orientation for the grating. Small mirrors direct the specific vibrational Raman bands of the major species (N_2 , O_2 , H_2 , H_2O , CO_2 , CO , and CH_4) onto seven PMTs mounted at the exit plane of the spectrometer. A 16-channel gated charge integrator measures and digitizes, with 12-bit resolution, the photocurrents from the PMTs and photodiode.

The possible Raman interferences arising from laser-induced fluorescence were monitored using three additional PMTs positioned at approximately the 590-, 615-, and 640-nm exit plane positions. These spectral regions have laser-induced fluorescence effects from the 532-nm excitation; in particular, fluorescence emissions from the C_2 Swan bands [26] onto the CO channel can give anomalously high CO measurements at fuel-rich conditions.

Properly accounting this effect is especially important for the inner-cone flame front of a Bunsen flame, which is known to have high levels of C_2 , as is evident from the observable C_2 chemiluminescence [27].

Laser-Induced Fluorescence Diagnostics

Figure 2 also shows the two frequency-doubled, Nd:YAG-pumped dye laser systems used to generate the ultraviolet (UV) wavelengths required for OH and NO excitation. The UV beams were overlapped onto the Raman probe volume at a small crossing angle. The measurement probe volume was defined by a kinematically removable, 800- μm pinhole located at the waist of the Raman-Rayleigh probe volume. By adjusting the 532-nm Raman and UV laser beams through the pinhole prior to each experiment, the proper alignment of the probe volumes with respect to the collection optics was consistently obtained. Telescopes were used to adjust the beam waists such that about 90% of the UV energy passed through the 800- μm pinhole; this approach maximizes the linear fluorescence range for the desired spatial resolution ($\sim 750\text{-}\mu\text{m}$).

Digital delay pulse generators time the firing sequence of the three lasers. The Raman and LIF lasers are each fired 150 ns apart, eliminating the interference between the Raman and two LIF channels. Time-resolved data on the order of a fraction of a microsecond were collected at the laser pulse repetition frequency of 10 Hz; however, the steady-state laminar nature of the Bunsen flame permitted averaging the single-shot data over a period of 20 s or 200 shots, thereby increasing the signal-to-noise ratio (SNR).

For the OH excitation, we tuned the frequency-doubled dye laser output to the $O_{12}(8)$ transition of the $A^2\Sigma^+ \leftarrow X^2\Pi(1,0)$ band of OH ($\lambda = 287.9\text{ nm}$). Use of this satellite transition reduces the absorption of the laser beam propagating through the flame, since its line-strength is substantially weaker than those of the main branch transitions. The OH and NO transitions were easily saturated with the available laser energies; consequently, to remain in the linear regime, we attenuated the UV beam for the OH excitation to approximately 40

$\mu\text{J/pulse}$ using neutral density filters. For the NO excitation, we tuned the second dye-laser to the $Q_1(18)$ transition of the $A^2\Sigma^+ \leftarrow X^2\Pi(0,0)$ band of NO ($\lambda = 225.9\text{ nm}$). This wavelength was generated by frequency doubling the output of the second dye laser ($\lambda = 286.8\text{ nm}$) and mixing it with the residual 1064-nm radiation from the Nd:YAG pump laser. This transition was selected because it is well populated at flame temperatures (as well as ambient temperatures) and avoids a significant amount of interference from the nearby vibrationally hot oxygen transitions in the $B^3\Sigma^+ \leftarrow X^3\Sigma^- (2,4)$ and $(5,5)$ bands. To ensure a linear-fluorescence regime, the laser energy used for the NO excitation was attenuated to approximately 10 $\mu\text{J/pulse}$.

The LIF signal from the probe volume was collected using a specially designed low f -number Cassegrain mirror-lens system. The reflective design eliminates the chromatic aberration present in transmissive lenses, permitting easy alignment and focusing of the different fluorescence wavelengths. A dichroic mirror separates the OH and NO fluorescence components, which are subsequently imaged onto the slits of two different PMTs fitted with color glass filters. For the detection of the OH fluorescence, we used Schott WG-295 and Hoya U-340 color glass filters, which reject the scattered radiation, and transmit the fluorescence from the dominant $(1,1)$ and $(0,0)$ bands ($295 < \lambda < 340\text{ nm}$). The fluorescence from the $(0,0)$ band results from the vibrational energy transfer (VET) from the $v' = 1$ to $v' = 0$ states [28]. For NO detection, we used Schott UG-5 color glass filters and a PMT with a solarblind photocathode; this combination effectively reduces scattered background radiation and permits broad band detection of the fluorescence from the NO, $v' = 0$, and $v'' = 1\text{--}5$ bands ($230 < \lambda < 300\text{ nm}$). Again, the slits in front of the PMTs defined the probe volume dimensions along the beam propagation axis and were adjusted to match those of the Raman-Rayleigh system.

Beamsplitters direct portions of the OH and NO laser beams to photodiodes for energy measurements. These secondary beams were also used in recording the LIF from two reference flames burning near-stoichiometric mix-

tures of CH₄ and air. The fluorescence signals from the reference flames permit the wavelength monitoring of the dye lasers throughout the experiment to ensure that they remain constant.

Raman Signal Calibration

In principle, Raman scattering provides a signal proportional to the number density of all the species being probed; however, the signals are also slightly modified by the following: increases in the temperature, which result in a broadening and shift of the vibrational bands; and the “crosstalk” between various vibrational and rotational bands of the different species. The most notable case is that of N₂ and O₂ which partially overlap with CO and CO₂, respectively. The temperature and crosstalk effects were accounted for through the calibration procedure. This involved recording the Raman signals over a wide range of known temperatures, gas compositions, and concentrations.

The calibrations include measurements in cold gases, lean and rich mixtures of H₂-air, H₂-CO-air, and CH₄-air flames burned above a non-premixed calibration burner. The non-premixed calibration burner (a so-called Hencken burner) was constructed from a bundle of small-diameter stainless-steel air and fuel tubes arranged in an alternating matrix; the separate fuel and air flows then burn as an array of small nonpremixed flames. This burner design prevents flashback problems associated with premixed H₂-air flames [15], and at locations sufficiently far downstream, most of the species (NO is an exception) are in local thermodynamic equilibrium. Thus, this burner provides a means of calculating the species concentration and temperature from the fuel-air flow rates [24].

Fluorescence Signal Calibration

For the OH and NO LIF measurements, the temperature and species concentrations measured by the Raman and Rayleigh scattering provide the necessary information for calculating the electronic quenching corrections. We employ the methodology described by Carter

and Barlow [23] for calculating the temperature and mixture dependent quenching corrections for OH and NO, using the quenching cross-sections provided by Paul [29] and Paul et al. [21]. The conversion of fluorescence signal to number densities, in general, requires: (1) the cross sections describing electronic quenching for all excited vibrational levels with specific colliders, and (2) the cross sections for the VET between the different excited vibrational levels. Currently, however, insufficient data exists for completely describing both the electronic quenching of the $v' = 1$ excited state and the VET between the $v' = 1$ and $v' = 0$ states of OH. Thus, for the OH quenching corrections, we approximate the temperature dependence of the net collisional de-excitation rate using the quenching rates for the $v' = 0$ state [29].

For the linear-fluorescence regime, the number density N (cm⁻³) of NO and OH is related to the fluorescence signal S_f through the relation

$$N = \left[\frac{N}{S_f} \right]_{\text{CAL}} \left(\frac{[F_B]_{\text{CAL}}}{F_B} \right) \left(\frac{[E_L/Q]_{\text{CAL}}}{[E_L/Q]} \right) \times \left\{ \frac{[g(\nu_0)]_{\text{CAL}}}{g(\nu_0)} \right\} S_f, \quad (2)$$

where F_B is the Boltzmann fractional population, E_L is the laser energy, Q is the overall collisional quench rate (s⁻¹), ν_0 is the transition frequency, $g(\nu_0)$ is the spectral overlap between the laser and the transition, and the subscript CAL refers to the calibration values [23]. The spectral overlap $g(\nu_0)$ was modeled using a Gaussian profile for the laser and a Voigt profile for absorption lineshape. The variation of the spectral overlap with temperature, however, was found to be minimal in these measurements.

The OH LIF calibration factor $[N/S_f]_{\text{CAL}}$, was obtained in a fuel-lean CH₄-air flame ($\phi = 0.94$) using the calibration burner in a premixed mode. The equilibrium OH number density was calculated using the Raman-Rayleigh measured temperature, which was typically only 10 to 30 K less than the adiabatic equilibrium value. For the NO calibrations, equilibrium calculations could not be used

since NO is typically far below equilibrium at reasonable distances above the burner. Additionally, the concentrations encountered in the calibration flame were too small for measurement using absorption. Consequently, we obtained the calibration factor $[N/S_f]_{\text{CAL}}$ using two fuel-lean ($\phi = 0.72$) $\text{CH}_4\text{-O}_2\text{-N}_2$ flames stabilized above a watercooled, sintered-bronze, flat-flame McKenna burner: one flame contains a known amount of NO that is substituted for a portion of the total N_2 . The two flames are otherwise identical; the Raman-Rayleigh measurements in the flames showed that the temperatures and concentrations differ by less than a percent between the two flames. By dividing the doped-NO number density by the difference of the two signals, a background-free calibration factor, $[N_{\text{doped}}/(S_{f\text{-doped}} - S_{f\text{-undoped}})]_{\text{CAL}}$ was obtained.

We verified the NO calibration procedure by measuring the LIF signal from an NO-doped room-temperature air flow; this doped-NO number density (deduced from the known air and NO flow rates) was then compared to the value resulting from Eq. 2 using the flame calibration factor $[N_{\text{doped}}/(S_{f\text{-doped}} - S_{f\text{-undoped}})]_{\text{CAL}}$ described above. The known and calculated number densities differed by only 7%. This difference is within the range of uncertainty for the quenching corrections (10%). Furthermore, we performed a one-dimensional flame calculation of the NO-doping procedure using a well established flame code [30, 31], in conjunction with the mechanism of Glarborg et al. [32] as modified by

Drake and Blint [33]. The results of the model showed that none of the doped-NO was destroyed by the flame front.

RESULTS

A series of CH_4 -air flames in the calibration burner operating with equivalence ratios ranging from 0.80 to 1.38 were used to check the measurement accuracy of the Raman-Rayleigh and OH LIF calibrations. Figure 3 shows the experimentally measured and calculated equilibrium (at the measured Raman-Rayleigh temperature) values of the N_2 , O_2 , H_2 , H_2O , CO_2 , CO , and OH concentrations. The Hencken calibration burner produced close-to adiabatic flames (the Raman-Rayleigh measured temperature was typically 15–25 K lower than predicted by adiabatic equilibrium). For single-shot Raman measurements, photon shot noise is the dominant source of uncertainty [15]. By time averaging over 200 shots, however, the precision and detection limits are increased. Based on the Rayleigh scattering signal RMS variance of about 1%, we estimate the precision of the single-shot temperature measurements to be ± 20 K at a temperature of 2000 K. The absolute temperature uncertainty however, is ± 36 K at a temperature of 2000 K—due mainly to the uncertainty in the calibration of the effective Rayleigh cross-section. As shown in Fig. 3, the measured major species concentrations agree well with the calculated (equilibrium) values. We estimate the

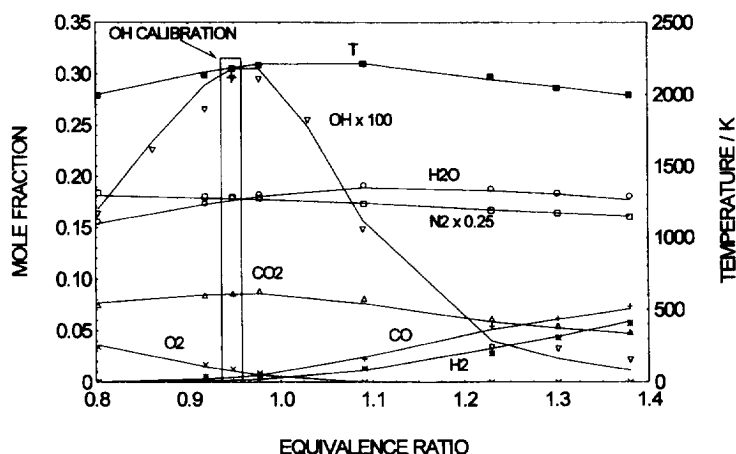


Fig. 3. Comparison of Raman-Rayleigh-LIF measurements (data points) with calculated equilibrium (lines) at the measured Raman-Rayleigh temperature for a series of premixed methane-air calibration flames. Note that the OH scale is magnified, and the N_2 scale is reduced.

time-averaged uncertainty of the major species measurements to be $\pm 3\%$ of full-scale for the different species (e.g., ± 0.024 mole fraction for N_2 in air). The uncertainty in the concentration measurements result mainly from uncertainties in the calibration procedure. For the OH calibration, we used the measured temperature ($T_{MEAS} = 2180$ K, whereas $T_{ADIA} = 2187$ K) to calculate the equilibrium OH value. With this single-point calibration, the measured OH at the other equivalence ratios differ with the equilibrium values by no more than 7% (for $\phi < 1.25$). This agreement is excellent considering the simplified treatment of the overall quenching corrections.

Figures 4–6 show the radial profiles of the Bunsen flame at different axial locations for flame A, $\phi = 1.38$ (see Table 1). Figure 4 details the radial profile across the “double-cone” Bunsen flame at the Z_1 axial location (Fig. 1). Figure 4 shows that the temperature rapidly rises from the cool unburned core to approximately 1980 K, where it plateaus between the inner and outer flame zones. As expected, the temperature reaches a maximum at the outer, stoichiometric flame zone (2077 K). The CO concentration (magnified by 10) peaks at the inner flame zone, coinciding with

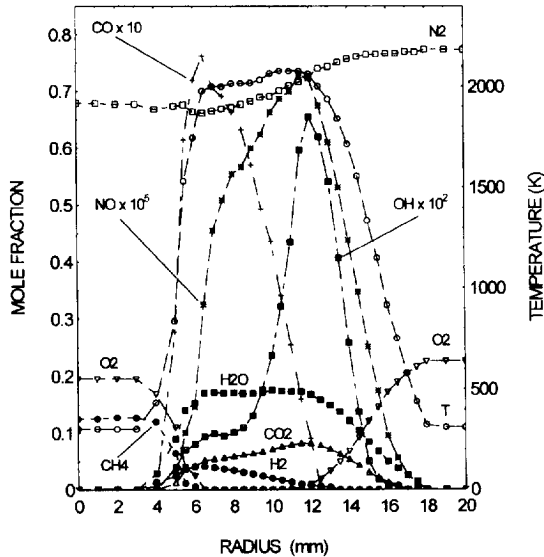


Fig. 4. Radial profiles for flame A ($\phi = 1.38$) at the Z_1 axial location (see Fig. 1). The CO, OH and NO scales are magnified for clarity. For reference, a mole fraction of 1.0 on the left axis corresponds to a NO concentration of 100 ppm.

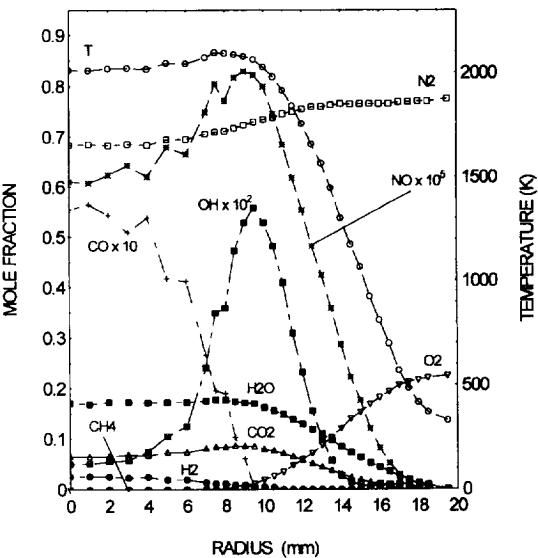


Fig. 5. Radial profiles for flame A at the Z_2 axial location, approximately 10 mm above the inner flame cone tip. Note that the small oscillations in the concentrations are due to disturbances to the flame from air currents in the laboratory.

the oxidation of CH_4 and appearance of H_2 . At this axial location, the measured inner-cone flame temperature is a little lower than predicted by the adiabatic equilibrium calculations ($T = 1996$ K) due to some radiative losses, but the measured CO concentration ($X_{CO} = 0.075$)

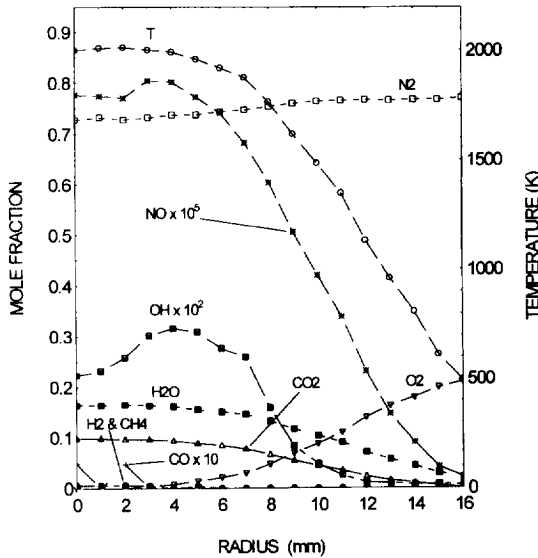


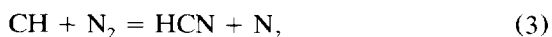
Fig. 6. Radial profiles for flame A at the Z_3 axial location, approximately 20 mm below the outer visible flame tip. At this axial location, the methane is completely consumed and the CO is barely detectable.

is slightly higher than that predicted by equilibrium ($X_{\text{CO}} = 0.071$). The OH (magnified by 100) peaks near the stoichiometric contour defined by the intersection of the H_2 and the O_2 concentration profiles.

Figure 4 also shows the radial NO profiles for flame A. The maximum NO concentration (72 ppm) at this axial position coincides with the location of maximum temperature. This results from the thermal NO mechanism which is important at temperatures above 2000 K [13]. The NO forms almost immediately beyond the inner flame zone (hence the term *prompt* NO), and increases linearly with radius.

Although the Bunsen flame is a two-dimensional flame, a rough estimate of the *peak* OH and CO concentrations and temperature at the inner flame front was obtained from the results of a one-dimensional flame model. We calculated profiles of the species of interest using an adiabatic premixed one-dimensional free methane-air flame model [30, 31, 34] incorporating the Miller and Bowman [9] reaction mechanism as modified by Frenklach et al. (49 species with 265 reactions) [35]. For the model inputs, we used a 300 K initial reactant temperature and the methane-air mixture specified in Table 1, flame A. Williams and Fleming [36] have successfully used this modeling approach for the prediction of radicals in NO-doped $\text{CH}_4\text{-O}_2\text{-N}_2\text{-Ar}$ low-pressure burner-stabilized flat-flames. For flame A, this model agrees well with the measured temperature and CO and OH concentration at the inner flame zone (T within 2%, OH within 5%). Of particular interest is the agreement of the superequilibrium CO peak discussed earlier: the model agrees within 1% with our measured values of $X_{\text{CO}} = 0.075$. Our one-dimensional model also shows that at the inner flame zone, there is a peak of superequilibrium O-atom concentration and CH radicals, located just upstream of the maximum temperature.

Our one-dimensional flame model, however, over-predicts the NO at the inner flame zone by about 15 ppm. Drake and Blint [33] reported that the predicted amount of NO is very sensitive to the rate constant of the reaction



considered the rate controlling step in the prompt NO pathway [9]. The uncertainty in this rate constant, together with the differences in the CH concentration and temperature between the one-dimensional model and the Bunsen flame may be the cause of this discrepancy. The measurements and numerical predictions reported by Reisel et al. [37] for laminar one-dimensional flat $\text{C}_2\text{H}_6\text{-O}_2\text{-N}_2$ flames, also show a tendency to overpredict the NO in fuel-rich flames.

Figure 5 shows the radial profile for flame A at the Z_2 axial location. This location is approximately 8 mm above the tip of the inner flame cone. The levels of NO are generally increasing, and reach a maximum value of about 82 ppm with a local minimum at the centerline. The temperature is relatively constant in the central portion of the flame and decreases rapidly past the outer flame zone defined by the peak OH location. Also note that the maximum value of the temperature is almost the same as at the Z_1 axial location. The CO peaks at the flame centerline and decreases monotonically with radius. We can also see that most of the H_2 and essentially all of the CH_4 has been consumed at this location.

Figure 6 shows the radial profile for flame A at the Z_3 axial location, which is approximately 20 mm below the visible tip of the outer flame cone. Here, the peak temperature has decreased slightly to about 2000 K. The centerline NO value has increased from 60 ppm to about 80 ppm. Note that the centerline OH values have also steadily increased with increasing axial distance. CO at this location was barely detectable using Raman scattering.

Figures 7–9 show the axial profiles along the centerline of the flames A, B, and C (equivalence ratios of 1.38, 1.52, and 1.70, respectively). Figure 7 shows the data for flame A and reveals in detail the trends observed in Figs. 5 and 6. We find that the temperature peaks just beyond the inner-cone flame tip at 2050 K and stays relatively constant at about 2000 K all the way to the visible outer cone flame tip (located at approximately 110 mm). Throughout this region, NO is steadily formed via the thermal mechanism and reaches a peak value of approximately 80 ppm at the outer

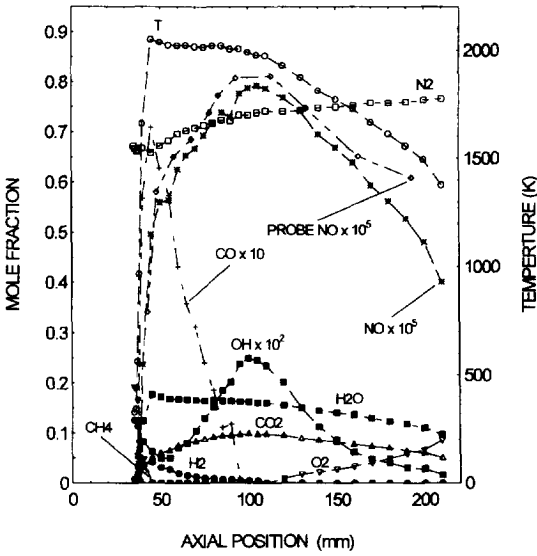


Fig. 7. Axial profiles along the centerline of flame A ($\phi = 1.38$). NO measurements using a quartz suction probe and chemiluminescent NO_x analyzer are also shown for comparison.

cone flame tip where it starts to decrease due to dilution.

We also measured the axial NO concentration for flame A using an uncooled quartz microprobe (3-mm diameter tapered to a 0.5-mm orifice diameter) and chemiluminescent

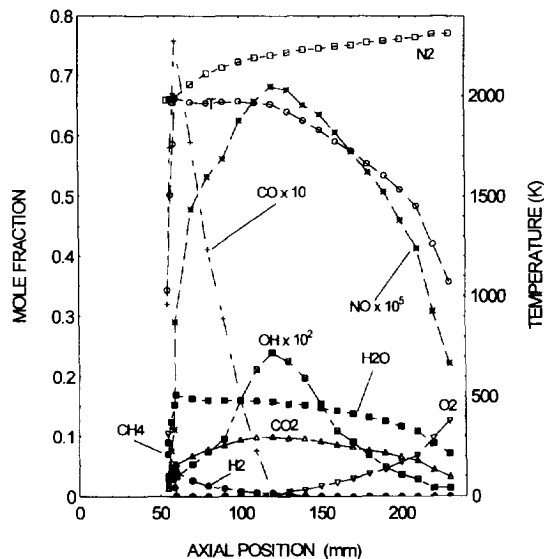


Fig. 8. Axial profiles along the centerline of flame B ($\phi = 1.52$).

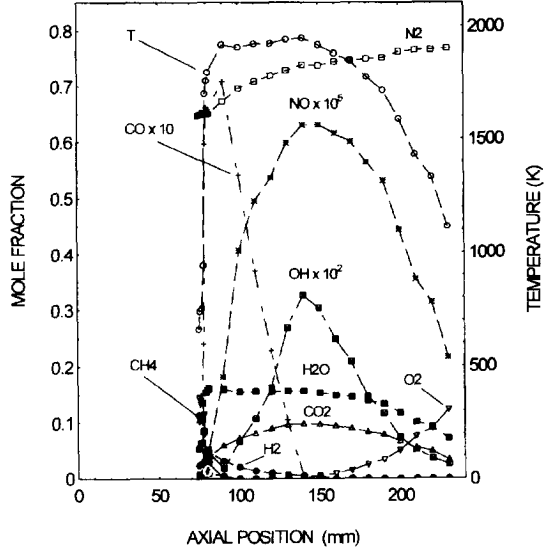


Fig. 9. Axial profiles along the centerline of flame C ($\phi = 1.70$).

NO_x analyzer; the probe measurements were of dry NO (a water trap was used), and thus we corrected the plotted NO concentration for water content using the Raman measurements. The water trap does not affect the probe sampling measurements of NO, as shown by Kramlich and Malte [38]. Figure 7 shows that the NO probe measurements (adjusted for water content) agree well with the LIF measurements. The good agreement between the two techniques reflects the accuracy of the quenching cross-sections and the calibration procedure. Although the high SNR of the NO measurements provide a single shot precision of 2% for the 80 ppm range, the uncertainty of the quenching corrections and the calibration limit the absolute uncertainty of the time-averaged NO values to $\pm 10\%$ or about 8 ppm.

We were able to use a suction probe for comparison in this instance due to the slow reactivity of NO with other combustion products [39]. Moreover, at this location, the intrusive effects of the probe on the flame properties are minimal because of the 1-dimensional nature of the flame at the centerline. The probe, however, could not be used for sampling the radial profiles shown in Figs. 4–6, since the flame zones were visually perturbed

by the probe tip due to the steep scalar gradients found in these 2-dimensional flame regions. Access to the chemiluminescent NO_x analyzer required performing the probe measurements with the burner mounted outside of the wind tunnel. This necessitated the use of a 300-mm-long, 70-mm-diameter quartz duct to isolate the flame from air currents in the laboratory. Consequently, the last few probe values diverge from the NO fluorescence data points due to the different entrainment and dilution effects existing at far-downstream axial locations.

Figure 8 shows the axial profiles for flame B ($\phi = 1.52$). The maximum NO concentration has decreased to about 68 ppm, at least in part, due to the slightly lower temperature. The peak temperature for this equivalence ratio is about 1900 K, which is 100 K higher than that predicted by adiabatic equilibrium. The superadiabatic temperature is the result of the preheating (through conduction and radiation) of the unburned air-fuel mixture by the coaxial outer flame zone. As the equivalence ratio increases, the height of the inner flame cone also increases, and the unburned air-fuel mixture has more time for preheating. Adiabatic equilibrium calculations that include the observed preheating of the initial reactants, result in temperatures similar to the peak measured temperatures. Thus the peak temperature in a Bunsen flame is relatively independent of the equivalence ratio and remains at about 2000 K.

Figure 9 shows the axial profile of flame C ($\phi = 1.70$). The temperature peaks at about 1900 K; this is about 140 K hotter than predicted by adiabatic equilibrium. At this highly fuel-rich condition, the distinction between the inner and outer flame zones was not as visually apparent, and this is reflected in the smoother temperature profile at the inner flame zone. The peak NO value has decreased to 63 ppm. The decrease in prompt NO with increasing equivalence ratio (for $\phi > 1.4$) is likely the result of the reduced CH concentration (see Eq. (3)). This is also evident from our one-dimensional flame calculations that show that the maximum CH-radical concentrations change from 3.7 ppm at $\phi = 1.38$, to only 0.11 ppm at $\phi = 1.70$.

CONCLUSIONS

Using a combination of Raman-Rayleigh scattering and LIF in a methane-air Bunsen flame, we have simultaneously measured the temperature, OH, NO, and the major species (N_2 , O_2 , H_2 , H_2O , CO_2 , CO, CH_4). We obtained both radial and axial profiles for three equivalence ratios (1.38, 1.52, and 1.70). In addition to obtaining an accurate and detailed mapping of temperature and species concentrations in a Bunsen flame, we found that as the equivalence ratio was increased from 1.38 to 1.70, the peak NO value decreased from 79 ppm to 63 ppm. We also found that using a one-dimensional premixed laminar flame model incorporating finite rate chemistry, satisfactorily predicts properties such as the temperature, and CO and OH concentrations at the inner flame zone.

Our measurements show that the axial flame temperatures are typically 100–150 K higher than that predicted by adiabatic equilibrium for reactants with an initial temperature of 300 K. We attribute this to the preheating of the unburned fuel-air mixture as it travels upwards into the conical flame zone surrounding it. The height of the inner-flame cone increases with increasing stoichiometry; hence, the amount of preheating also increases with stoichiometry, offsetting the effect stoichiometry on flame temperature. Consequently, the maximum centerline temperatures in a Bunsen flame (about 2000 K) were insensitive to the stoichiometry.

The authors would like to thank the following people for their contributions: Mr. Tom Prast for his help with the Raman-LIF apparatus; Mr. Bradley Edgar for his expertise and assistance with the suction probe measurements of NO; Mr. Marc Rumminger for his calculations of the one-dimensional premixed flame used in comparison with the inner Bunsen flame zone; and Prof. John Reisel for his calculations of the one-dimensional NO-doped flames used in the LIF calibrations. Q.V.N. and R.W.D. were supported in part by the California Institute for Energy Efficiency; C.D.C. was supported by the Wright Laboratory, Aero Propulsion and Power Directorate under Contract F33615-92-2202; G.J.F. and R.S.B. were supported by the U.S. Department of Energy,

Office of Basic Energy Sciences, Division of Chemical Sciences.

REFERENCES

- Correa, S. M., *J. Prop. Power* 8:1144–1151 (1992).
- Norton, T. S., Smyth, K. C., Miller, J. H., and Smooke, M. D., *Combust. Sci. Technol.* 90:1–34 (1993).
- Baulch, D. L., and Drysdale, D. D., *Combust. Flame* 23:215–225 (1974).
- Westbrook, C. K., and Dryer, F. L., *Prog. Ener. Combust. Sci.* 10:1–57 (1984).
- Nguyen, Q. V., Edgar, B. L., Dibble, R. W., and Gulati, A., *Combust. Flame* 100:395–406 (1995).
- Bowman, C. T., *Twenty-Fourth Symposium (International) on Combustion*, The Combustion Institute, Pittsburgh, 1992, pp. 859–878.
- Zeldovich, Ya. B., *Acta Physicochem. USSR* 21:557 (1946).
- Fenimore, C. P., *Combust. Flame* 19:289 (1972).
- Miller, J. A., and Bowman, C. T., *Prog. Ener. Combust. Sci.* 15:287–338 (1989).
- Drake, M. C., Ratcliffe, J. W., Blint, R. J., Carter, C. D., and Laurendeau, N. M., *Twenty-Third Symposium (International) on Combustion*, The Combustion Institute, Pittsburgh, 1990, p. 387.
- Bachmeier, F., Eberius, K. H., and Just, Th., *Combust. Sci. Technol.* 7:77 (1973).
- Thorne, L. R., Branch, M. C., Chandler, D. W., Kee, R. J., and Miller, J. A., *Twenty-First Symposium (International) on Combustion*, The Combustion Institute, Pittsburgh, 1986, pp. 965–977.
- Heard, D. E., Jeffries, J. B., Smith, G. P., and Crosley, D. R., *Combust. Flame* 88:137–148 (1992).
- Reisel, J. R., and Laurendeau, N. M., *Combust. Sci. Technol.* 98:137–160 (1994).
- Dibble, R. W., Masri, A. R., and Bilger, R. W., *Combust. Flame* 67:189–206 (1987).
- Barlow, R. S., and Carter, C. D., *Combust. Flame* 97:261–280 (1994).
- Crosley, D. R., *J. Chem. Phys.* 93:6273 (1989).
- Heard, D. E., Jeffries, and Crosley, D. R., *Chem. Phys. Lett.* 178:533–537 (1991).
- Thoman Jr., J. W., Gray, J. A., Durant Jr., J. L., and Paul, P. H., *J. Chem. Phys.* 97:8156–8163 (1992).
- Drake, M. C., and Ratcliffe, J. W., *J. Chem. Phys.* 98:3850–3865 (1993).
- Paul, P. H., Gray, J. A., Durant Jr., J. L., and Thoman Jr., J. W., *AIAA J.* 32:1670–1675 (1994).
- Hirano, A., Ricoul, F., and Tsujishita, M., *Jpn. J. Appl. Phys.* 32:3300–3307 (1993).
- Carter, C. D., and Barlow, R. S., *Opt. Lett.* 19:299–301 (1994).
- Barlow, R. S., Dibble, R. W., Chen, J. Y., and Lucht, R. P., *Combust. Flame* 82:235 (1990).
- Nguyen, Q. V., Dibble, R. W., Hoffman, D., and Kampmann, S., *Ber. Bunsenges. Phys. Chem.* 97:1634–1642 (1993).
- Faust, W. L., Goldberg, L. S., Craig, B. B., and Weiss, R. G., *Chem. Phys. Lett.* 83:265 (1981).
- Glassman, I., *Combustion*, Academic, Orlando, FL, 1987, p. 331.
- Smith, G. P., and Crosley, D. R., *Appl. Opt.* 22:1428 (1983).
- Paul, P. H., *J. Quant. Spectrosc. Radiat. Transf.* 51:511–524 (1994).
- Kee, R. J., Grcar, J. F., Smooke, M. D., and Miller, J. A., Sandia Report SAND85-8240, Sandia National Laboratories, Livermore, CA, 1985.
- Kee, R. J., Rupley, F. M., and Miller, J. A., Sandia Report SAND89-8009B, Sandia National Laboratories, Livermore, CA, 1989.
- Glarborg, P., Miller, J. A., and Kee, R. J., *Combust. Flame* 65:177–202 (1986).
- Drake, M. C., and Blint, R. J., *Combust. Sci. Technol.* 75:261 (1991).
- Kee, R. J., Dixon-Lewis, G., Warnatz, J., Coltrin, M. E., and Miller, J. A., Sandia Report SAND86-8246, Sandia National Laboratories, Livermore, CA, 1986.
- Frenklach, M., Wang, H., Bowman, C. T., Hanson, R. K., Smith, G. P., Golden, D. M., Gardiner, W. C., and Lisianski, V., 1994, *Twenty-Fifth Symposium (International) on Combustion*, The Combustion Institute, Work in Progress Poster No. 26, Session 3.
- Williams, B. A., and Fleming, J. W., *Combust. Flame* 98:93–106 (1994).
- Reisel, J. R., Carter, C. D., and Laurendeau, N. M., submitted to: Eighth International Symposium on Transport Phenomena in Combustion, 1994.
- Kramlich, J. C., and Malte, P. C., *Combust. Sci. Technol.* 18:94–104 (1978).
- Bowman, C. T., and Seery, D. V., *Emissions from Continuous Combustion Systems*, Plenum, New York, 1972, p. 123.

Received 21 March 1995; revised 3 October 1995